# Impression

lundi 10 mai 2021 12:34

# Elastic-frustration-driven unusual magnetoelastic properties in a switchable core-shell spin-crossover nanostructure

Yogendra Singh,[1] Hassane Oubouchou,[2] Masamichi Nishino,[3,5] Seiji Miyashita,[4,5] and Kamel Boukheddaden[1,*]

[1]*Groupe d'Etudes de la Matière Condensée, Université de Versailles, Université Paris-Saclay, 78035 Versailles, France*

[2]*Ecole Polytechnique d'Architecture and d'Urbanisme, El Harrach 16000, Algeria*

[3]*Research Center for Advanced Measurement and Characterization, National Institute for Materials Science, Tsukuba, Ibaraki 305-0047, Japan*

[4]*Department of Physics, Graduate School of Science, The University of Tokyo, Bunkyo-Ku, Tokyo 113-0033, Japan*

[5]*Elements Strategy Initiative Center for Magnetic Materials, National Institute for Materials Science, Tsukuba, Ibaraki 305-0047, Japan*

(Received 3 October 2019; revised manuscript received 23 December 2019; accepted 13 January 2020; published 11 February 2020)

Spin-crossover (SCO) solids have been studied for their fascinating properties, exhibiting first-order phase transitions and macroscopic bistabilities, accompanied by significant magnetic, structural, and optical changes. These exceptional properties make these materials promising for applications as high-density information storage and optical switches. Recently, the critical progress made in chemistry allowed the design of spin-crossover nanocomposites, combining the properties of two types of spin-crossover solids having different properties, like different lattice parameters, bulk moduli, transition temperatures, ligand fields, etc. In this paper, we consider a microscopic electroelastic description of a SCO nanostructure made of a SCO active core surrounded by a SCO active shell, for which we impose an unconventional elastic frustration at the core-shell interface. The detailed examination of the thermodynamic properties of such a nanocomposite, as a function of the lattice parameter misfit between the two constituents, revealed that the frustration causes unexpected behaviors on the thermal dependence of the average bond lengths, such as the emergence of two- or three-step spin transitions, with self-organization of the spin states in the plateau regions. These results highlight the nontrivial character of the magnetoelastic properties in switchable SCO nanoparticles.

DOI: 10.1103/PhysRevB.101.054105

## I. INTRODUCTION

The thermally induced spin-crossover (SCO) transitions between the low-spin (LS) and the high-spin (HS) states of Fe(II) complexes with suitable ligands are typical examples of switchable molecular solids. They have been studied [1–9] for many years for their promising applications as pressure sensors [10], displays [11], data storage, and molecular switches [12]. During the last decade, compounds with multistep spin conversion remained quite rare and have attracted increasing attention in theoretical and experimental studies [13–18], due to their possible capability to build up a 3-bit electronics.

Multistep SCO behavior results from structural ordering or/and the existence of multistability in the molecule itself, like in binuclear SCO systems [19,20]. In contrast, some multistep SCO systems consist of an asymmetric unit containing two or more nonequivalent sites [21,22], having different local environments. At the macroscopic scale, the competition or the interplay between the two types of SCO sites manifests through the existence of an intermediate phase associated with partial conversion from HS to LS states. It is worth noticing that the processing of SCO materials with two inequivalent sites is hardly controllable, and most of the time the behavior of the high-spin fraction is hardly predictable. That is why, recently, chemists started designing well controllable and reproducible SCO core-shell nanocomposites, made of two SCO materials, with the objective of combining the SCO properties of different constituents [23]. Interest in finite-size effects properties [24–27], and in the manipulation [28], design, and visualization [29] of small objects at the nanoscale, is rapidly growing thanks to the development of adapted experimental tools (electronic and atomic force microscopy, high-resolution x-ray diffraction, etc.).

With the development of nanotechnologies and the availability of experimental results, core-shell nanocomposites have attracted considerable attention also from the theoretical point of view. To this end, several models have been proposed to investigate the size effect in SCO materials. Among them, the well-known Ising-like model [30] has been applied to study size effects on the first-order spin transition as well as other aspects related to first-order-reversal-curves technique [31], using Monte Carlo (MC) simulations [32]. More recently, we used this model on a square system, solved by a MC simulation under specific boundary conditions [33], in which we have investigated the lattice architecture effects [34]. Surface and size effects also have been studied in a one-dimensional (1D) spin-phonon model [35] and also for hollow particles [24,36]. Further, we have developed an electroelastic model [37] which takes into account the coupling

*kamel.boukheddaden@uvsq.fr

 

between the spin state change of the molecule (from LS to HS) and the local molecular volume, which is equivalent to ones already designed by Nishino *et al.* [38] and Enachescu *et al.* [39], and other models that included the role of surface relaxations [40,41] and particle environment [42–44]. Quite recently, we extended the electroelastic model to the case of SCO nanoparticles [45], in which we considered that the SCO atoms at the surface were kept in the HS state, due to their coordination to water molecules, which decrease their ligand field. As a result, the thermal hysteresis moved according to the atomic surface-volume ratio, in good agreement with the experiments. Later, a specific electroelastic model was designed to incorporate the case of core-shell SCO nanoparticles, made of an active SCO core and an inert shell, where we investigated the detailed properties of the SCO core as a function of the elastic properties (rigidity, lattice parameter misfit, and size) of the shell [43,46–52].

Quite recently, experimental investigations on SCO nanocomposites have been performed by several groups [14,53–58]. For example, Wang *et al.* [14]. have succeeded in growing high-quality spin-crossover nanocomposites by mixing two kinds of SCO materials, in heteroepitaxial conditions, namely, $[Fe(NH_2\text{-}trz)_3](BF_4)_2$ and $[Fe(Htrz)_2(trz)](BF_4)$, which have different SCO properties. The former has a transition temperature $T_1 = 260$ K and a hysteresis width of 4 K, while the latter shows a transition temperature $T_2 = 368$ K and an associated thermal hysteresis width of 46 K. Thus, these two materials have different ligand fields and most likely different strength of cooperativity between the molecules. In the aforementioned experiment, the core is constituted by the material which has the smaller ligand field (thus the lower transition temperature), which is covered by the second material (stronger ligand field). The magnetic studies of the formed nanocomposite clearly showed the occurrence of two transition temperatures on heating, located at 288 and 314 K. It is then observed that the transition temperature of the first constituent (the core) increased by 28 K while that of the second material (the shell) decreased by 54 K, due to the elastic interplay between the core and the shell structures. Furthermore, a very gradual and third transition involving a small fraction of molecules occurs at 347 K. This third transition was attributed to the occurrence of mixture of material. So, the present study of the active core-shell nanoparticles is realized by Monte Carlo simulations, conducted on spin and lattice positions in two-dimensional (2D) lattices with square symmetry for simplicity.

Core and shell are allowed to switch thermally between LS and HS states and have different ligand fields. We have chosen the core and shell to have equal lattice parameters in the LS state, while they are different in the HS state. Moreover, an elastic frustration is considered at the interface, by imposing for the interface bonds antagonist values depending on whether the considered atom belongs to the core or shell parts. Elastic parameters are kept the same for both core and shell in both LS and HS states. We investigate the effect of this lattice misfit in order to study their mechanical (average lattice parameters) and electronical (HS fractions) responses around the transition region with respect to temperature. In this exploratory paper, we consider a core with a higher ligand field than that of the shell. The objective here is to draw predictions on the influence of the magnetoelastic coupling in switchable SCO nanostructures, looking for unprecedented thermal behaviors of the HS fraction lattice parameter, emerging from the interplay between the SCO transitions of the core and the shell constituting the nanoparticle.

The paper is organized as follows: in Sec. II, we present the model, describe the simulation technique, and justify the choice of $T_{eq}$ for core and shell; Sec. III is devoted to the presentation and discussion of the obtained results; and in Sec. IV we conclude and outline some possible developments in the present paper.

## II. THE MODEL

An example of a core-shell structure is schematized in Fig. 1(a). The core has a square shape containing $N_C \times N_C$ sites and the shell has the shape of a thick frame of width $N_s$ surrounding all the core. As a result, the number of shell atoms is $(N_C + 2N_S)^2 - N_C^{[2]} = 4\,N_S(N_C + N_S)$, and the total number of atoms of the nanocomposite is $N_{\text{tot}}^2$, where $N_{\text{tot}} = N_C + 2N_S$.

Each core or shell site, $i$, may have two states, HS or LS, with respective fictitious spin values $S_i = +1$ (HS) and $S_i = -1$ (LS). The present model includes the change of the local volume of the SCO molecules during their switching from one state to the other.

Each atom located at site "$i$" is described by its spin state $S_i$ and its coordinates $(x_i,\ y_i)$. The atoms are constrained to be in the plane. The position and spin state change in the MC simulation depend on the energetic situation. The reader can find a review of the original electroelastic model for which we have already discussed in detail some of its thermodynamic properties in recent works [45,59,60].

The Hamiltonian [33] describing the core-shell system is written as

$$H = H_{\text{core}} + H_{\text{shell}} + H_{\text{inter}}, \tag{1}$$

where the core and shell contain electronic ($H_{\text{core}}^{\text{elec}}$ and $H_{\text{shell}}^{\text{elec}}$) and elastic ($H_{\text{core}}^{\text{elast}}$ and $H_{\text{shell}}^{\text{elast}}$) contributions, while the interface has only elastic interactions, written as follows:

$$H_{\text{core}}^{\text{elec}} = \sum_i \frac{1}{2}[\Delta_c - k_B T \ln g] S_i, \tag{2a}$$

$$H_{\text{core}}^{\text{elast}} = A_c \sum_{(i,j)}^{nn} \left[r_{ij} - R_0^C(S_i, S_j)\right]^2 + B_c \sum_{(i,k)}^{nnn} \left[r_{ik} - d_0^C(S_i, S_k)\right]^2, \tag{2b}$$

$$H_{\text{shell}}^{\text{elec}} = \sum_i \frac{1}{2}[\Delta_S - k_B T \ln g] S_i, \tag{3a}$$

$$H_{\text{shell}}^{\text{elast}} = A_S \sum_{(i,j)}^{nn} \left[r_{ij} - R_0^S(S_i, S_j)\right]^2 + B_S \sum_{(i,k)}^{nnn} \left[r_{ik} - d_0^S(S_i, S_k)\right]^2, \tag{3b}$$

$$H_{\text{inter}}^{\text{elast}} = \frac{1}{2}\left(H_{\text{inter}}^{C,\text{elast}} + H_{\text{inter}}^{S,\text{elast}}\right) \tag{4a}$$

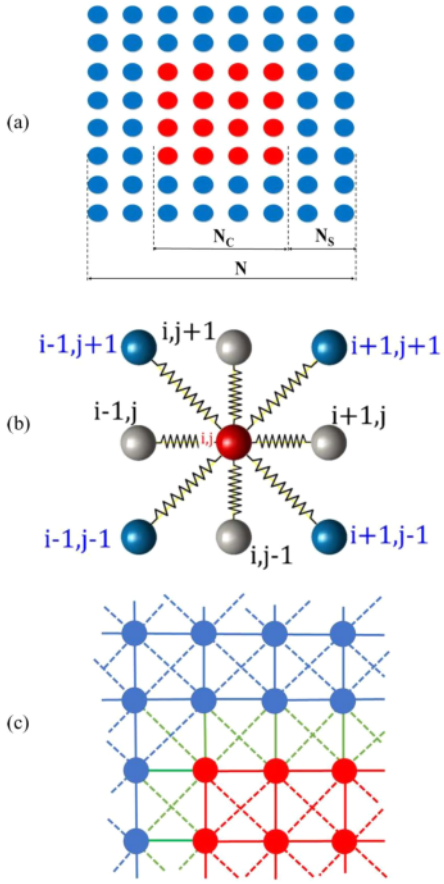


FIG. 1. (a) Schematic structure of the SCO nanocomposite. Blue and red dots are two spin-crossover sites belonging to different materials. (b) The configuration of the elastic interactions in the two-dimensional square model considered in this paper showing a central red ball connected by springs to gray and blue sites, representing the nearest and next-nearest neighbors, respectively. (c) The blue, green, and red solid lines denote $R_0^S(S_i,S_j)$, $R_0^{\rm int}(S_i,S_j)$, and $R_0^C(S_i,S_j)$, respectively. The blue, green, and red dashed lines denote $d_0^S(S_i,S_j)$, $d_0^{\rm int}(S_i,S_j)$, and $d_0^C(S_i,S_j)$, respectively. As a reference lattice, we take $R_0^S(-1,-1)=R_0^{\rm int}(-1,-1)=R_0^C(-1,-1)=1$ ($R_{0,S}^{\rm LL}=R_{0,C}^{\rm LL}=R_{0,\rm int}^{\rm LL}=1$).

where

$$H_{\rm inter}^{C,\rm elast}=A_{\rm int}\sum_{(i,j)}^{nn}\left[r_{ij}-R_{0\,C-S}^{\rm int}(S_i,S_j)\right]^2+B_{\rm int}\sum_{(i,k)}^{nnn}\left[r_{ik}-d_{0\,C-S}^{\rm int}(S_i,S_k)\right]^2, \tag{4b}$$

$$H_{\rm inter}^{S,\rm elast}=A_{\rm int}\sum_{(i,j)}^{nn}\left[r_{ij}-R_{0\,S-C}^{\rm int}(S_i,S_j)\right]^2+B_{\rm int}\sum_{(i,k)}^{nnn}\left[r_{ik}-d_{0\,S-C}^{\rm int}(S_i,S_k)\right]^2. \tag{4c}$$

Hamiltonians given in Eqs. (2a) and (2b) [Eqs. (3a) and (3b)] account exclusively for the energetic contribution of core (shell) atoms only. The elastic interface energy [Eq. (4a)] is split into two contributions related to the core [Eq. (4b)] and the shell [Eq. (4c)] parts. Here, we consider that at the interface a core imposes to its neighboring shell atoms its equilibrium distances, and vice versa for the shell. The situation is somewhat similar to that of two adversaries sharing the same extended border in which each party considers that it belongs to him.

In the Hamiltonians of core (2a) and shell (3a), the first term expresses the effective ligand field energy ($\Delta_c$ for the core and $\Delta_s$ for the shell) and that of the entropy effects, $k_BT\ln g$, where $g$ is the degeneracy ratio between the HS and the LS states, which is assumed here as the same for both constituents and temperature independent. $A_C$ and $B_C$ ($A_S$ and $B_S$) are the elastic constants of the core (the shell) of the first nearest neighbors (NNs) and the next-nearest neighbors (NNNs), respectively. Similarly, the elastic constants in the interface region are noted by $A_{\rm int}$ and $B_{\rm int}$ and are considered the same whatever the nature (core or shell) of the considered atom. In addition, to reduce the number of free parameters in the model, we have chosen $A_C=A_S=A_{\rm int}$ and $B_C=B_S=B_{\rm int}$.

To account for the volume change at the transition obtained in experimental structural studies [61], which reported relative lattice expansions of ≈1–5%, the equilibrium bond lengths (the equilibrium distance) between two neighboring sites depend on their spin states, as already introduced in a previous work [37]. Here, the molecules interact via elastic springs [see Fig. 1(b)]. The equilibrium bond lengths are denoted $R_0^x(S_i,S_j)$ [$d_0^x(S_i,S_k)$ for two NN (NNN) atoms $S_i,S_j$ ($S_i,S_k$). For the core and the shell bonds, they are given by

$$R_0^x(S_i,S_j)=R_{0,x}^{\rm HL}+\frac{\delta_R^x}{4}(S_i+S_j), \tag{5a}$$

$$d_0^x(S_i,S_k)\sqrt{2}\left[R_{0,x}^{\rm HL}+\frac{\delta_R^x}{4}(S_i+S_k)\right], \tag{5b}$$

where $x=C,\ S$ stands for the core and shell, respectively. The quantities $R_{0,x}^{\rm HL}$ and $\delta_R^x$ are, respectively, the NN equilibrium distance in the HS-LS configuration and the misfit between the lattice parameters of the HS and LS phases [$\delta_R^x=R_0^x(+1,+1)-R_0^x(-1,-1)$], where, $x=S,C$.

These quantities are obtained as a function of the different lattice parameters, $R_{0,x}^{\rm HH}=R_0^x(+1,+1)$, $R_0^{\rm HL}=R_0^x(+1,-1)$, and $R_0^{\rm LL}=R_0^x(-1,-1)$, as follows:

$$R_{0,x}^{\rm HL}=\frac{R_{0,x}^{\rm HH}+R_{0,x}^{\rm LL}}{2}, \tag{6a}$$

$$\delta_R^x=\left(R_{0,x}^{\rm HH}-R_{0,x}^{\rm LL}\right). \tag{6b}$$

Where HH, HL and LL stand for HS-HS, HS-LS, and LS-LS neighbors, respectively. For interface bonds, made of core and shell atoms, the equilibrium bond lengths, $R_{0\,C-S}^{\rm int}(S_i,S_j)$ [$R_{0\,S-C}^{\rm int}(S_i,S_j)$] where $S_i$ is the spin state of the core (shell) site and $S_j$ is that of the shell (core), are given by

$$R_{0\,x-y}^{\rm int}(S_i,S_j)=R_{0,x}^{\rm HL}+\frac{\delta_R^x}{4}(S_i+S_j), \tag{7a}$$

$$d_{0\,x-y}^{\rm int}(S_i,S_k)=\sqrt{2}\left[R_{0,x}^{\rm HL}+\frac{\delta_R^x}{4}(S_i+S_k)\right], \tag{7b}$$

where $(x, y) = (C, S)$ or $(S, C)$ provides information about the location (core or shell) from which the bond is considered. The quantities $R^{\mathrm{HL}}_{0,x}$ and $\delta^x_R$ are the same as those defined in Eqs. (6a) and (6b).

In the Monte Carlo simulations, the system is warmed up from $T = 5$ to 200 K (390 K for $R^{\mathrm{HH}}_{0,S} = 1.0$) in steps of increment 1 K, and then cooled down to the initial temperature. At each temperature step we evaluate the HS fraction, $n_{\mathrm{HS}}$, that is, the fraction of molecules occupying the HS state, given by

$$n_{\mathrm{HS}} = \frac{1 + \langle S \rangle}{2}, \tag{8}$$

where $\langle S \rangle$ is the average value of the spin state and the average NN distance, $\langle r \rangle$, is defined as

$$\langle r \rangle = \frac{\sum_{i \neq j} \sqrt{(x_i - x_j)^2 + (y_i - y_j)^2}}{N^x_b}, \tag{9}$$

where $N^{\mathrm{tot}}_b = 2N_{\mathrm{tot}}(N_{\mathrm{tot}} - 1)$ is the total number of bonds. These two quantities, which can be viewed as order parameters characterizing the electronic and the elastic state of the system, are calculated for the core $N^c_b = 2N_c(N_c - 1)$, the shell $N^s_b = 2N_s(N_s + 2N_c - 1)$, and the whole lattice. Description and explanation related to the numerical procedure leading to solving Hamiltonian (1) are given in Sec. I of the Supplemental Material (SM) [62].

In a previous work [63], we have considered the study of a core-shell SCO nanoparticle, schematically represented in Fig. 1(a), where both constituents are active from the point of view of spin transitions. There, we studied the effect of the shell thickness on the thermal properties of the core and the shell as well. In this previous work, we assumed equal lattice parameters of the core and shell in their respective HS and LS states.

## III. RESULTS AND DISCUSSIONS

### A. Thermal behavior of the uncoated core and hollow shell

The analysis of the thermodynamic properties of this spin-crossover nanostructure showed the existence of an efficient mechanical coupling between the core and the shell moieties, which influences the thermodynamic behavior of each other. Due to this mechanical coupling, the temperature dependence of the total nanocomposite is far from the sum of each of its constituents. Indeed, according to the difference of transition temperatures and elastic interactions between core and shell, the whole nanocomposite may lead to several possibilities of spin transitions (two-step, gradual, one step with thermal hysteresis, etc.) as a result of an interplay between the electroelastic properties of both constituents, resulting in a complex distribution of pressure (or elastic energy) inside the lattice. In the first part of this paper, we started with the thermal investigations of the uncoated SCO core of size $N_c \times N_c = 40 \times 40$ and hollow shell of the same size and five-layer thickness. The parameter values used throughout this paper are, for the core part, $\Delta_C = 450$ K, $g$ (degeneracy ratio)$= 150$, and $A_C = B_C = 10^5$ K nm$^{-2}$ and, for the shell, $\Delta_S = 200$ K and $A_S = B_S = 10^5$ K nm$^{-2}$. For simplicity, the equilibrium bond lengths between nearest-neighboring atoms of spin configurations HS-HS, HS-LS, and LS-LS were considered as, respectively, equal to 1.05, 1.025, and 1.0 nm for the core. For the present simulations on the uncoated shell, the equilibrium distances between LS-LS, HS-LS, and HS-HS nearest neighbors are taken equal to 1.03, 1.015, and 1.0 nm, respectively.

The transition temperatures of the isolated core (shell) are given by the relation $T^C_{\mathrm{eq}} = \frac{\Delta_C}{k_B \ln g} \sim 90$ K ($T^S_{\mathrm{eq}} = \frac{\Delta_S}{k_B \ln g} \sim 40$ K). As a reference, Fig. 2 summarizes the temperature dependences of the HS fraction of the shell [Fig. 2(a)] and core [Fig. 2(b)], which undergo first-order phase transitions, accompanied by thermal hysteresis. Moreover, one can easily see that the transition temperatures arising from the MC simulations are confirmed to be the ones predicted by the simple relation $T_{\mathrm{eq}} = \frac{\Delta}{k_B \ln g}$.

### B. Case of an active core and shell spin-crossover nanostructure

Now we turn to the case of the spin-crossover nanocomposite, schematically represented in Fig. 1(a), in which core and shell consist of active spin-transition materials. For that, we decorate the uncoated core of Fig. 2(b) by the hollow spin-crossover shell [Fig. 2(a)], of five-layer thickness ($N_S = 5$). The Monte Carlo procedure used to solve the thermodynamic properties of this composite system is the same as that used for the uncoated core.

In the MC simulations, a lattice site is randomly selected. This site is inside the core (i.e., surrounded by core atoms only) or inside the shell (i.e., surrounded by shell atoms only) or at the interface, belonging to the core or shell parts. If the atom is inside the core or the shell, we calculate its elastic energy using Hamiltonians (2b) and (3b), combined with the spin dependence of equilibrium distances, given in expressions (5a) and (5b). In contrast, in the interface region, if we select in the MC process a site belonging to the core (shell) part, its elastic energy is calculated using Eq. (4b) [Eq. (4c)] with the corresponding equilibrium distances given by Eq. (7a) [Eq. (7b)]. This constraint causes an elastic frustration that deploys over the lattice, the consequences of which are discussed below.

#### *1. Effect of the core-shell lattice parameter misfit on the whole system*

In the previous work [63], we stated that the core and the shell have the same equilibrium bond lengths in HS and LS states. In the present paper, we take $R^{\mathrm{HH}}_{0,S}$ as a variable, which causes a change: $R^{\mathrm{HL}}_{0,S} = \frac{R^{\mathrm{HH}}_{0,S} + R^{\mathrm{LL}}_{0,S}}{2}$.

Now let us summarize the situation: $R^{\mathrm{LL}}_{0,S} = R^{\mathrm{LL}}_{0,C} = 1$ and $R^{\mathrm{HH}}_{0,C} = 1.05$ are kept invariant while $R^{\mathrm{HH}}_{0,S}$ changes from the value of $R^{\mathrm{LL}}_{0,C}$ to that of $R^{\mathrm{HH}}_{0,C}$. The values of all NN lattice distances are summarized in Table I. Owing to the 2D character and square symmetry of the lattice, the NNN equilibrium distances corresponding to the electronic configurations given in Table I are obtained from the NN equilibrium distances multiplied by $\sqrt{2}$.

Now, we focus on the imposed equilibrium distances at the core-shell interface. It can be easily checked that the core-shell interface contains $4N_C$ NN bonds and $4(2N_C - 1)$ NNN bonds.

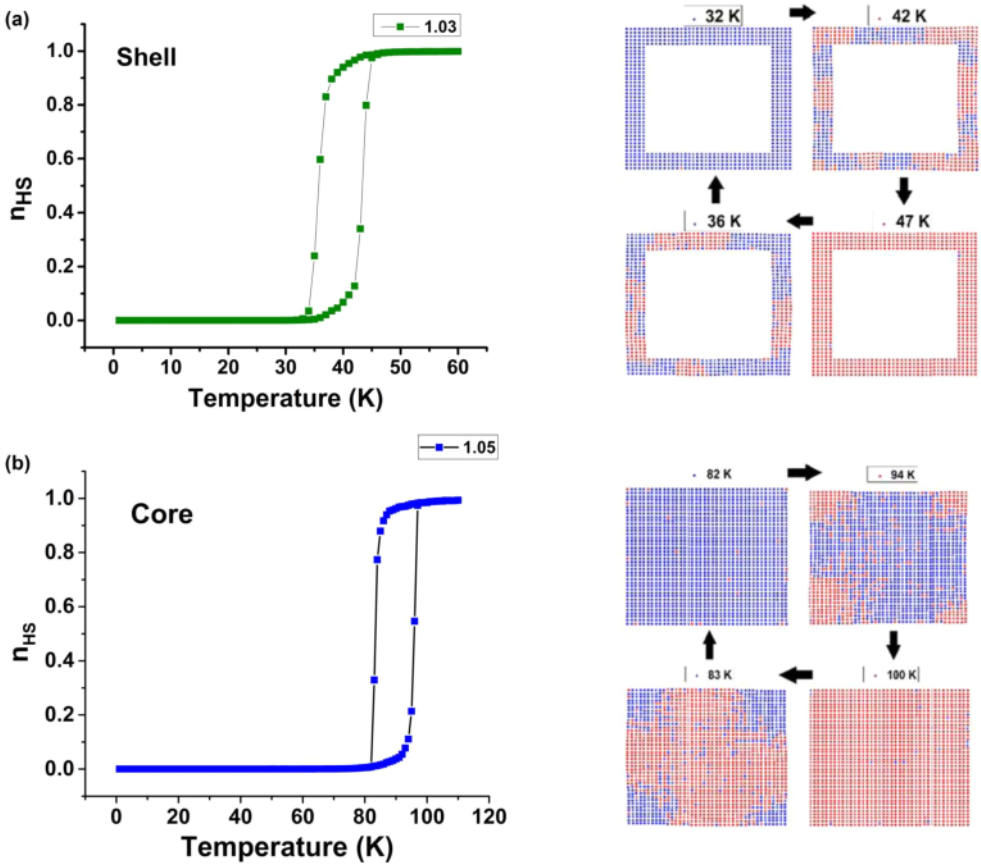


FIG. 2. Thermal variation of the HS fractions and lattice parameters of the uncoated 2D hollow (a) and core (b) nanoparticle (with square symmetry). The core size is 40 × 40 and the hollow shell has five-layer thickness. The equilibrium NN distances in HS-HS, HS-LS, and LS-LS configurations are, respectively, equal to 1.05, 1.025, and 1.0 nm for the core and 1.03, 1.015, and 1.0 nm, for the shell. For both cases, the spatial distributions of the HS (red dots) and LS (blue dots) sites along the spin transition phenomenon are shown in the right panels.

It is important to stress here the individual definition of the equilibrium distances, $R_0^{\text{int}}(S_i, S_j)$, at the core-shell interface. In a previous work [63], where the equilibrium NN distances of HH, HL, and LL configurations were the same for the core and the shell, those of the interface were simply calculated as the average values of those of core and shell atoms taking into account their spin states. Here, we consider a different scenario, for which the equilibrium bond lengths at the interface are summarized in Table I. Thus, a chosen atom belonging to the core-shell interface and located in the core side wants to impose to its NN (or NNN) shell atom the equilibrium core bond length and similarly for shell atoms. Within this condition, bonds at the interface viewed from the core (shell) have the equilibrium bond lengths $R_0^C(S_i, S_j)$ $[R_0^S(S_i, S_j)]$, given in Table I. As a result, the same bond at the core-shell interface is asked to have the equilibrium distance of the core (shell)

TABLE I. Equilibrium NN distances used for the core, shell, and core-shell bonds. The HS shell NN bond length ($R_{0S}^{\text{HH}}$) is used here as a variable.

| NN configurations (nm) | HH | HL | LL |
|---|---|---|---|
| Core NN distance | $R_{0,C}^{\text{HH}} = 1.05$ | $R_{0,C}^{\text{HL}} = \frac{1+R_{0,C}^{\text{HH}}}{2} = 1.025$ | $R_{0,C}^{\text{LL}} = 1.0$ |
| Shell NN distance | $R_{0,S}^{\text{HH}}$ | $R_{0,S}^{\text{HL}} = \frac{1+R_{0,S}^{\text{HH}}}{2}$ | $R_{0,S}^{\text{LL}} = 1.0$ |
| NN distance at the interface viewed from the shell | $R_{0,S}^{\text{HH}}$ | $R_{0,S}^{\text{HL}} = \frac{R_{0,S}^{\text{LL}}+R_{0,S}^{\text{HH}}}{2}$ | $R_{0,S}^{\text{LL}} = 1.0$ |
| NN distance at the interface viewed from the core | $R_{0,C}^{\text{HH}} = 1.05$ | $R_{0,C}^{\text{HL}} = \frac{R_{0,S}^{\text{LL}}+R_{0,C}^{\text{HH}}}{2} = 1.025$ | $R_{0,C}^{\text{LL}} = 1.0$ |

when calculating the energy of the core (shell) atom. For example, an HS-LS interface bond constituted of a HS core site and a shell LS site has the apparent equilibrium distance $R_{0\,C-S}^{\rm int}(+1,-1) = \frac{R_{0,C}^{\rm LL}+R_{0,C}^{\rm HH}}{2}$ (=1.025 nm) from the point of view of the core side and $R_{0\,S-C}^{\rm int}(-1,+1) = \frac{R_{0,S}^{\rm LL}+R_{0,S}^{\rm HH}}{2}$ when viewed from the shell side. When the value of $R_{0,S}^{\rm HH}$ is different from that of $R_{0,C}^{\rm HH}$ an elastic frustration immediately takes place at the core-shell interface in bonds unless its connecting sites are not in the LS state, as it appears in Table I, where we summarize the expressions of the different equilibrium distances corresponding to the various bond configurations in the core, shell, and interface regions.

Simulations are performed for different values of the equilibrium lattice parameter of the shell in the HS phase, going from $R_{0,S}^{\rm HH} = 1.05$ nm (NN bond length value of the core in HS) to $R_{0,S}^{\rm HH} = 1.0$ nm (NN bond length value of the core in LS). The change in $R_{0,S}^{\rm HH}$ values cause the change of HL configurations of the shell as well as those of HH and HL configurations of core-shell bond lengths, located in the interface region. The other lattice parameters are kept invariant, as shown in Table I.

Thus, we now examine the general situation where the nanocomposite is made of two SCO materials having different HS lattice parameters. Due to the elastic nature of the spin transition phenomenon, it is expected that this difference of the lattice parameter between the core and the shell will play an important role in the thermal behavior of the HS fraction of the whole system.

The results of the simulations are summarized in Fig. 3, which reports the thermal variation of the total HS fraction and average lattice parameter of the whole nanocomposite for various values of $R_{0,S}^{\rm HH}$. It is observed that the change in $R_{0,S}^{\rm HH}$ affects the thermal behavior of the entire system. This is due to the fact that the elastic interaction energy, $\Delta E$, responsible for the SCO transition of the shell, depends on the lattice parameter misfit inside the shell between the LS and HS states: $\Delta E = \frac{1}{2}(A_S + 2B_S)(\delta_R^S)^2 = \frac{1}{2}(A_S + 2B_S)(R_{0,S}^{\rm HH} - R_{0,S}^{\rm LL})^2$. These changes are then mechanically communicated to the core through the core-shell interface. Thus, the decrease in $R_{0,S}^{\rm HH}$ shifts the whole thermal response of the system to higher temperature, and causes interesting behaviors on the thermal dependence of the average bond lengths, which transforms through several steps. The origin of this behavior will be discussed in the next section, where we examine individually the thermal behavior of the core and the shell.

### 2. *Thermal properties of shell and core components*

Now, we examine the thermal behavior of the electronic and mechanical responses of the core and the shell separately as a function of $R_{0,S}^{\rm HH}$. Figure 4 shows the thermal dependences of the average HS fraction and the average lattice distance, $\langle r\rangle_S$, of the shell [Figs. 4(a) and 4(b)] for different $R_{0,S}^{\rm HH}$ values going from 1.05 to 1.00 nm (i.e., from $R_{0,C}^{\rm HH}$ to $R_{0,C}^{\rm LL}$), while $R_{0,S}^{\rm LL}$, $R_{0,C}^{\rm LL}$, $R_{0,C}^{\rm HH}$, and $R_{0C}^{\rm HL}$ are kept invariant as given in Table I. The associated HS fraction and lattice spacing, $\langle r\rangle_C$, of the core are depicted in Figs. 4(c) and 4(d), respectively.

It is interesting to mention that, for used $R_{0,S}^{\rm HH}$ values, the HS fraction of the shell [Fig. 4(a)] has a large plateau for $R_{0,S}^{\rm HH} = 1.00$, 1.02, and 1.03 nm which drastically reduces for $R_{0,S}^{\rm HH} = 1.04$ and almost disappears for $R_{0,S}^{\rm HH} = 1.05$. The existence of this plateau caused by the misfit between the equilibrium NN distance of the core, $R_{0,C}^{\rm HH} = 1.05$, and that of the shell, $R_{0,S}^{\rm HH}$, originates from the mechanical compressive strain exerted by the LS core on the shell. This prevents its complete transformation during the thermal transition process. As a consequence, the average shell NN distance in the HS state decreases [Fig. 4(b)] as $R_{0,S}^{\rm HH}$ decreases, leading to delay of the transition temperature of the core, the volume expansion of which between LS and HS states is hindered by the shell. On the other hand, for $R_{0,S}^{\rm HH} < 1.05$, the expansion or the contraction of the shell during its first-step transition is accompanied by the systematic contraction of the core [Fig. 4(d)], while its expansion starts only when its corresponding HS fraction increases [Fig. 4(c)]. This behavior

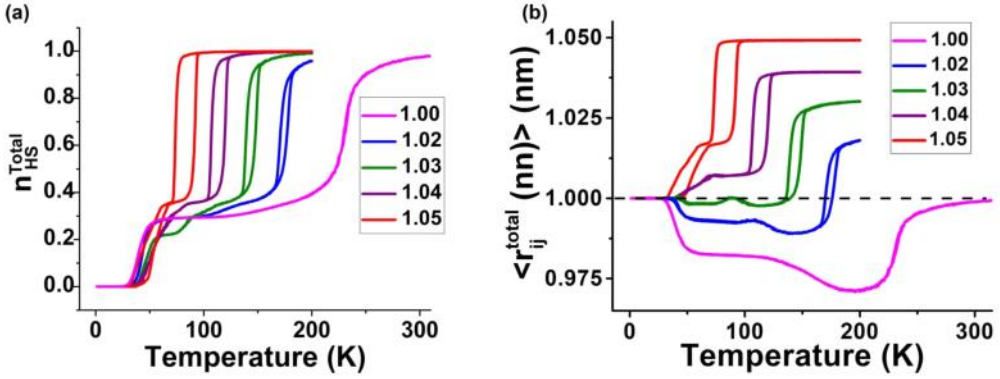


FIG. 3. Thermal variation of (a) the total HS fraction and (b) the average lattice parameter of the whole SCO nanocomposite for different equilibrium lattice parameters of the shell, which was varied from $R_{0S}^{\rm HH} = 1.00$ to 1.05 nm. The other lattice parameter values are given in Table I. The used values of the elastic constants are $A_C = A_S = A_{\rm int} = 10^5$ K nm$^{-2}$ for NN interactions and $B_C = B_S = B_{\rm int} = 10^5$ K nm$^{-2}$ for the NNN interactions in the core (C), shell (S), and interface (int).

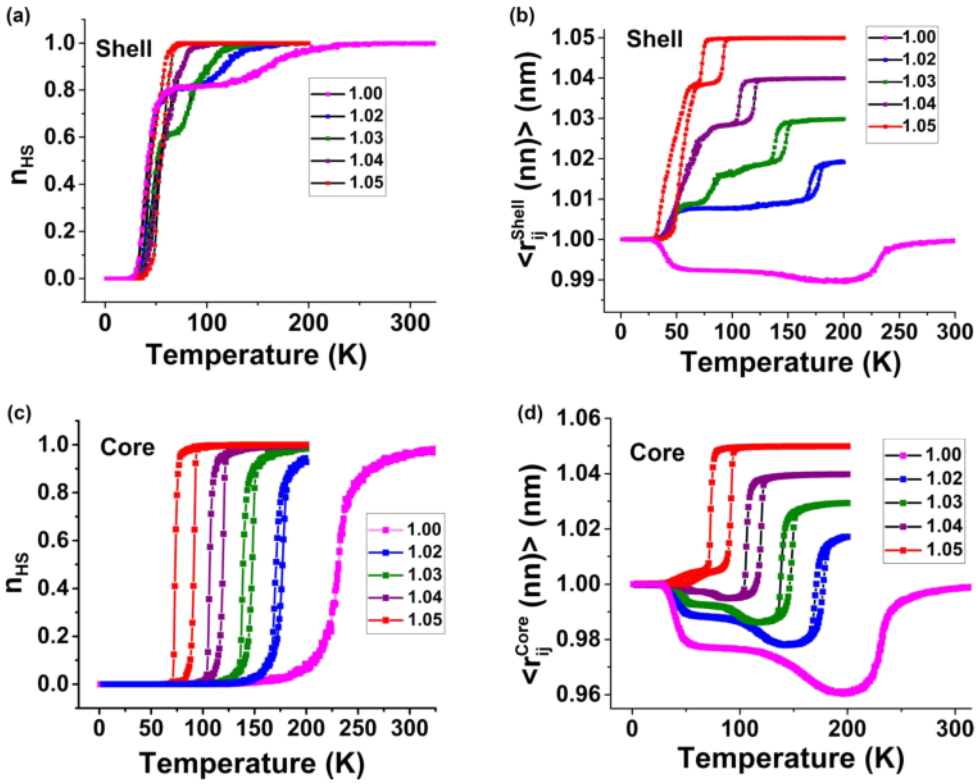


FIG. 4. Thermal variation of (a) the shell HS fraction and (b) the average NN distance for different $R_{0S}^{HH}$ values, varied from $R_{0S}^{HH} =$ 1.0 to 1.05 nm. (c, d) The temperature dependences of the core HS fraction and average NN distance for the same $R_{0S}^{HH}$ values. The other lattice parameter values are given in Table I. The other model parameters are given in the text.

indicates that the first contractions of the core are the result of its mechanical response to the shell's behavior.

Interestingly, while the first transition temperature of the shell shows only a slight shift towards 50 K as a function of $R_{0,S}^{HH}$ [see Fig. 4(a)], that of the core, displayed in Fig. 4(c), is significantly affected. That is, the center of the thermal hysteresis moves from 75 to ∼230 K, by decreasing $R_{0,S}^{HH}$ from 1.05 to 1.00 nm. Due to this critical change, the thermal hysteresis width of the core diminishes from 17 to 0 K.

Furthermore, it is clear from Fig. 4(a) that the HS fraction of the shell makes the transition in one step for $R_{0,S}^{HH} =$ 1.05 nm which converts to two steps with a plateau for $R_{0,S}^{HH} = 1.04,\ 1.03,\ 1.02$, and 1.0 nm, while the temperature dependences of the average bond length, $\langle r \rangle$, depict a double step transition for all $R_{0,S}^{HH}$. The first step is related to an incomplete electronic transformation of the shell due to compressive strain induced by the core which is still in the LS state, while the second step, which takes place around 70 K for $R_{0,S}^{HH} = 1.03$, for example, relates to the change in the bond lengths of the shell, which hardly reach their equilibrium values in the HS state as $R_{0,S}^{HH}$ decreases.

An interesting situation arises from the comparison between the thermal dependence of the HS fraction [Fig. 4(a)] and the bond lengths of the shell, shown in Fig. 4(b). The temperature dependence of the bond lengths of the shell exhibits thermal hysteresis for $R_{0,S}^{HH} = 1.02,\ 1.03$, and 1.04, which is absent in the thermal behavior of the HS fraction. In addition, as previously indicated, more marked plateaus appear in Fig. 4(b), compared to those of Fig. 4(a). This situation is even more pronounced for the core part where the temperature dependence of the HS fraction [Fig. 4(c)] giving the temperature dependence of the HS fraction, $n_{HS}$, shows a single-step first-order transition for $R_{0,S}^{HH} = 1.05,\ 1.04,\ 1.03,\ 1.02$ while the corresponding average core NN distance leads to multistep transitions [Fig. 4(d)].

This point is important and demonstrates that the magnetic response can be silent on the interplay between the structural changes of the core and the shell. Indeed, the behavior of the HS fraction of the core [Fig. 4(c)] is blind regarding the multistep transitions occurring in the core bond lengths [Fig. 4(d)], which are mostly sensitive to the changes of elastic parameters of the shell [Fig. 4(a)]. This point contrasts with the usual elastic models of SCO where the HS fraction and the average bond lengths are linked linearly [46].

It is worth noticing that the temperature dependence of the average core bond length shows very unusual and nonmonotonous trends around the temperature region of the transition of the shell. These behaviors are unique and of merit to be discussed in a detailed way.

To thoroughly understand the unconventional thermal behavior of $\langle r \rangle$ in Fig. 4(d), for $R_{0,S}^{\mathrm{HH}} \geqslant 1.04$, one has to consider that the expansion of the shell part during its phase transition induces tensile stresses on the core. For equal equilibrium HS lattice parameters of core and shell (i.e., $R_{0,S}^{\mathrm{HH}} = R_{0,C}^{\mathrm{HH}} = 1.05$ nm), the two subsystems form a unique and uniform elastic lattice (same bond lengths and elastic constants in LS and HS states). As a result, a ferroelastic interaction takes place between the shell and the core. Indeed, the first expansion of the shell [Fig. 4(b)] below 70 K is accompanied by an expansion of the core [Fig. 4(d)]. That is, the average NN distance of the core increases monotonously with temperature from the value of the LS state ($R_{0,C}^{\mathrm{LL}} = 1.0$ nm) to that of HS ($R_{0,C}^{\mathrm{HH}} = 1.05$ nm), with the presence of a small plateau around $T = 75$ K (on heating) at which $\langle r \rangle_C$ reaches the value 1.005. This effect is attributed to the transition of the shell thus causing a negative pressure on the LS core's lattice. It is worth mentioning that this plateau is hardly visible in the temperature dependence of the core HS fraction of Fig. 4(c).

In contrast, for $1.00 \leqslant R_{0,S}^{\mathrm{HH}} \leqslant 1.04$, the first expansion of the shell, on heating, induces a compressive stress on the core, which then contracts [see Fig. 4(d)]. This contraction continues as long as the core HS fraction keeps the value $n_{\mathrm{HS}} = 0$ [Fig. 4(c)]. When the HS fraction of the core starts to increase (due to thermal effects), $\langle r \rangle_C$ goes through a minimum and finally increases towards the value $R_{0,S}^{\mathrm{HH}}$ instead of $R_{0,C}^{\mathrm{HH}}$ ($> R_{0,S}^{\mathrm{HH}}$). In that sense, the core remains under high compressive pressure even in the HS state.

The observed contractions of the core are also due to the strong lattice misfit existing between the core and the shell lattice spacing. It is essential to mention that the amplitude of this core contraction also depends on the ratio of core and shell elastic constants, which are taken in the present case as equal to 1. Thus, a more compressible core may show significant mechanical responses, while a rigid one will prevent the transition of the shell. This exciting aspect will be investigated in a further work.

On the other hand, the thermal behavior of the average shell and core bond length [Figs. 4(b) and 4(d)] clearly demonstrates that for small lattice spacing of the HS shell the transition temperature is shifted upwards, recalling the effect of pressure on SCO materials. Indeed, it is important to keep in mind that, on heating, the shell makes the LS to HS transition before the core. As a result, when the shell reaches the HS state, two different processes emerge: (i) the core experiences compressive or tensile stress depending on the misfit lattice parameter and (ii) the expansion of the core lattice under the inhibited boundary conditions set by the shell part which in turn prevents the conversion of the core, which needs space to expand all the bond lengths. Thus, it delays the emergence of the thermally induced spin-state switching, which appears at higher temperature.

So, to summarize, the weak effect of the core on the shell lattice parameter [Fig. 4(b)] is attributed to the existence of a free surface of the shell, which allows relaxing of elastic strain. For example, for the case $R_{0,S}^{\mathrm{HH}} = 1.02$ nm, the shell switches from LS to HS (the corresponding average NN distances of which are 1.0 and $\approx$1.02 nm) around $T_S^{eq} \simeq 41$ K, which is very close to the transition temperature of the isolated shell, given by $T_S^{eq} = \frac{\Delta_S}{k_B \ln g} = 40$ K. In contrast, the behavior of the core part with $R_{0,C}^{\mathrm{HH}} = 1.05$ nm and $R_{0,C}^{\mathrm{LL}} = 1.0$ nm is significantly affected by the change of $R_{0,S}^{\mathrm{HH}}$, particularly when the misfit ($R_{0,C}^{\mathrm{HH}} - R_{0,S}^{\mathrm{HH}}$) increases. Several observations can be drawn: (i) the transition temperature of the core is clearly shifted to higher temperatures; (ii) depending on the value of $R_{0,S}^{\mathrm{HH}}$, the temperature dependence of the average core lattice parameter may follow a nonmonotonous trend; (iii) the thermal hysteresis width progressively vanishes with decreasing the $R_{0,S}^{\mathrm{HH}}$ values. In Fig. S.1 of SM [62] we can clearly see the correlation between the HS state of the core and shell with respect to the average lattice parameter of the shell and core.

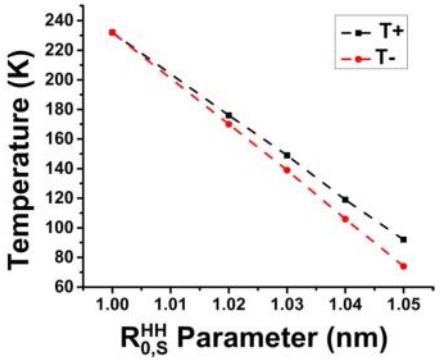


FIG. 5. High-spin shell lattice parameter dependence of the upper ($T^+$) and lower ($T^-$) transition temperatures of the core components, showing a clear vanishing of the thermal hysteresis for below the value, $R_{0,S}^{\mathrm{HH}} = 1.01$ nm, as a result of pressure effects exerted by the shell on the core due to the lattice parameter misfit.

To confirm the pressure effect of the shell on the transition of the core, we analyze the dependence of the upper and lower core transition temperatures on $R_{0,S}^{\mathrm{HH}}$ in Figs. 4(c) and 4(d). It shows (see Fig. 5) a clear linear trend, reminiscent of the behavior of SCO systems under an applied isotropic pressure [64], $P$, following the law $T_{\mathrm{eq}}^0(p) = \frac{2\Delta}{k_B \ln g} + \frac{p|\Delta V|}{k_B \ln g}$, and $|\Delta V|$ is the volume change between LS and HS states. In Fig. S.2 of SM [62] we can observe that when the whole system is in the HS state the differences between the average instantaneous bond length and the corresponding equilibrium distances for the shell and core in the HS state ($\langle r \rangle_{\mathrm{shell}}$) and ($\langle r \rangle_{\mathrm{core}}$) clearly show that the core is under a large stress compared to the shell, thus confirming the fact that the relaxation of the core lattice is obstructed by the HS shell lattice, which in turn shifts the transition temperature of the core to higher temperature.

### C. Spatial distribution of the HS fraction and evidence of labyrinth formation inside the core

Here we analyze the spatial dependence of the HS fraction in the core and the shell along with the thermal hysteresis of Fig. 4 and discuss the effect of lattice misfit, $R_{0,S}^{\mathrm{HH}} - R_{0,C}^{\mathrm{HH}}$, on the nucleation mode of the HS fraction. Selected snapshots depicting the spatial distribution of the HS fraction are presented in Fig. 6 for the values $R_{0,S}^{\mathrm{HH}} =$

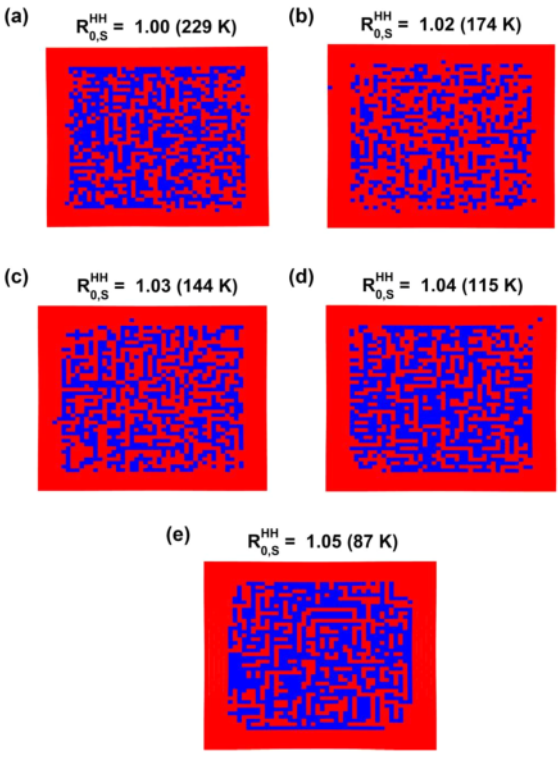


FIG. 6. Selected snapshots depicting the spatial distribution of the HS fraction presented in Figs. 4 and 5 for the case $R^{HH}_{0,S} = 1.00$, 1.02, 1.03, 1.04, and 1.05nm and temperature $T =$ 229, 174, 144, 115, and 87 K, respectively. The corresponding HS fraction (0.60, 0.52, 0.47, 0.43, 0.40) and lattice parameter (0.98, 0.99, 1.00, 1.01, 1.01) values can be easily read in Figs. 4(c) and 4(d) for the core lattice and Figs. 3(a) and 3(b) for the shell lattice. Note the emergence of labyrinth HS structures inside the core as a result of the spatial distribution of the strain. Here HS (in red) and LS (in blue) depict total HS occupation in the shell, and spatial distribution of the HS fraction in the core.

1.00, 1.02, 1.03, 1.04, and 1.05 nm and temperature $T =$ 229, 174, 144, 115, and 87 K, respectively. According to Fig. 4, this corresponds to the situation where the interplay between the elastic properties of the core and the shell is maximum. At these temperatures, the shell exerts highly anisotropic constraints on the system, which results in special spatial self-organization of the spin states through labyrinth structures (see Fig. 6) during the growth of the HS fraction. Such behavior is very interesting and could be correlated to the lattice shape and the spatial distribution of the elastic strain in the lattice. The formation of HS and LS stripes is attributed here to the coexistence of directional ferroelastic and antiferroelastic interactions, which can also be evidenced by the spatial behavior of the average lattice parameter inside the lattice. In addition, the fact that these 1D structures can be formed along both $x$ and $y$ directions indicates the absence of any anisotropic effects in the growth modes of these strings.

#### *1. Spatial profiles of the lattice bond lengths*

To get more insights about the magnetoelastic interplay between the electroelastic properties of the core and the shell, we monitor the spatial distribution of the atomic bond lengths along a horizontal line located at the middle of the lattice (at coordinate $j = \frac{N}{2}$) in the case of a HS shell and LS core, for several values of $R^{HH}_{0,S}$. The results are summarized in Fig. 7, which indicates that with $R^{HH}_{0,S}$ values between 1.0 and 1.04 the core experiences a strong nonuniform compressive stress along the $x$ direction [Figs. 7(a)–7(d)], which increases as $R^{HH}_{0,S}$ decreases, enhancing the elastic misfit at the core-shell interface. In contrast, for $R^{HH}_{0,S} = 1.05$ nm [Fig. 7(e)], we observe that the central part of the core experiences tensile stress while at the lattice borders a residual weak compressive stress remains. On the other hand, the shell part shows that the outer layers (close to the surface) are always under tensile stress, while the inner layer (close to the interface) is always under compressive stress, whatever the $R^{HH}_{0,S}$ value. More precisely, one may notice that for all cases shown in Fig. 7, or for shell layers close to the surface, the distance between successive sites, $d_{ij}$, is bigger than the equilibrium value, $R^{HH}_{0,S}$, which means that the shell is under tensile stress. For $R^{HH}_{0,S} = 1.0$, only the shell layer at the interface with the core experiences the compressive stress ($d_{ij} \simeq 0.98 < R^{HH}_{0,S}$). However, as $R^{HH}_{0,S}$ value increases, other inner shell layers start to feel the compressive strain exerted by the elastic core-shell misfit, as clearly depicted in Figs. 7(b)–7(e) through the number of red points situated below the dashed line indicating the $R^{HH}_{0,S}$ value. Similarly, the behavior of the LS core crucially depends on $R^{HH}_{0,S}$. For $1.00 \leqslant R^{HH}_{0,S} \leqslant 1.04$ nm, the NN distances, $d_{ij}$, along the considered horizontal line in the core are always smaller than $R^{HH}_{0,S}$, denoting that the core is under compressive stress. However, it is interesting to notice the nonuniform character of the spatial dependence of the distance, $|d_{ij} - R^{LL}_{0,C}|$, along the core's center. This quantity indeed decreases in a symmetric way when coming from both sides, meaning that the center of the core experiences weaker compressive stress, compared to the outer core layers located at the core-shell interface. As a result, the formation of HS core species from the outer core layers is prevented, at the benefit of the core center part. In addition, it is clearly seen in Fig. 7 that the amplitude of this compressive stress decreases as the value of $R^{HH}_{0,S}$ increases. This effect is important and helps in the formation of long HS strings at the origin of the emergence of the labyrinth structures, obtained for all $R^{HH}_{0,S}$ values, as depicted in Fig. 6. However, it is worth noticing that the lengths of the HS string forming the labyrinth, as well as the topology of the latter, depend on $R^{HH}_{0,S}$ values. Indeed, for the case $R^{HH}_{0,S} = 1.05$ nm, the central part of the core experiences now tensile stress ($d_{ij} > R^{LL}_{0,C}$) which enhances the HS string's length inside the core.

#### *2. Lattice distortion and spatial distribution of elastic stresses*

Now we focus on the stresses generated by the nucleation and growth process, which is important in the self-organization of the HS and LS states. For that, we determine the displacement field, $\vec{u}(i, j)$, associated with the lattice site,

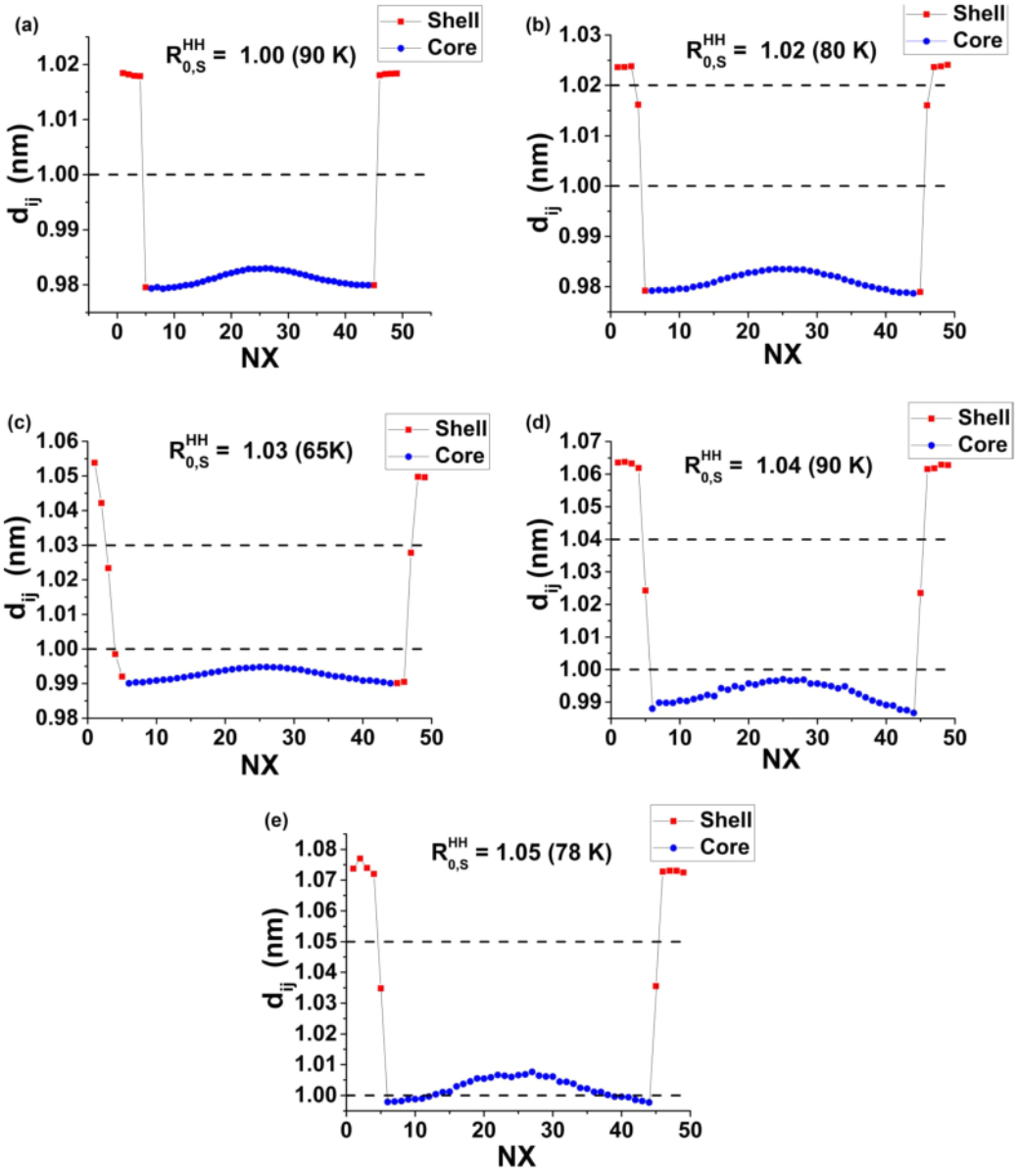


FIG. 7. Lattice parameter profile along a horizontal line located at coordinate $j = \frac{N}{2}$, in the middle of the lattice, for several HS shell lattice parameters, and temperatures corresponding to the plateau regions of Figs. 4(b) and 4(d). The data of the HS shell part are represented with red squares and those of the LS core part are represented with blue filled circles. All curves correspond to a LS core surrounded by a HS shell. The horizontal dashed lines, corresponding to $d_{ij} = R^{HH}_{0S}$ and $d_{ij} = 1.0$ nm, are, respectively, associated with the equilibrium bond lengths of the HS shell and LS core.

$(i, j)$, given by

$$\vec{u}_{ij} = \vec{r}_{ij} - \vec{r}^{\,0}_{ij}, \tag{10}$$

where $\vec{r}^{\,0}_{ij}$ and $\vec{r}_{ij}$ are the initial and final atomic positions of the site $(i, j)$. In the present analysis, we used the positions in the perfect LS state of the whole nanostructure as a reference state, because it is common to all the simulations. We have calculated the displacement field and its spatial distribution, of the core and shell atoms, for several values of $R^{HH}_{0,S}$ for the cases of Fig. 7. The obtained results are summarized in Fig. 8, and correspond to selected electroelastic snapshots in the plateau regions. Overall, they are in agreement with the conclusions drawn from Fig. 7. First, Fig. 8(a) corresponds

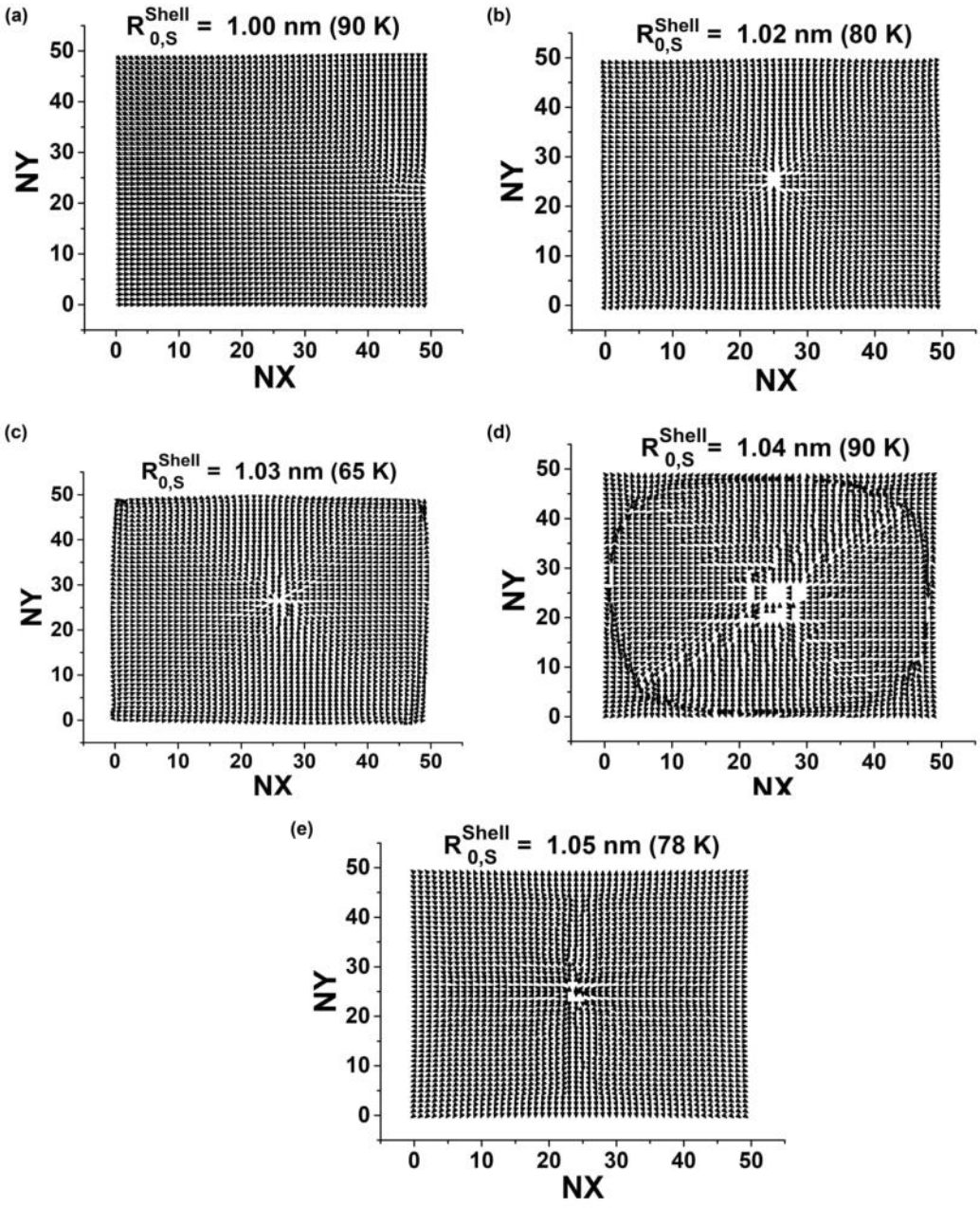


FIG. 8. Displacement fields for the different HS shell lattice parameter values (a) $R_{0,S}^{\mathrm{HH}} = 1.00$ nm, (b) $R_{0,S}^{\mathrm{HH}} = 1.02$ nm, (c) $R_{0,S}^{\mathrm{HH}} = 1.03$ nm, (d) $R_{0,S}^{\mathrm{HH}} = 1.04$ nm, and (e) $R_{0,S}^{\mathrm{HH}} = 1.05$ nm, corresponding to the situations depicted in Figs. 7(a)–7(e). The LS state, common to all figures, was used as a reference state for the calculations of the displacement field [see Eq. (9)].

to the situation where $R_{0,S}^{\mathrm{HH}} = 1.0$. Compared to Figs. 8(b)–8(e), it shows a loss of center symmetry, which is attributed to the randomly selected electronic configuration, which is affected by the fluctuations of the spin states induced by the stochastic aspect of the MC procedure. On the other hand, Figs. 8(b) and 8(c), corresponding, respectively, to $R_{0,S}^{\mathrm{HH}} = 1.02$ and 1.03 nm, show strong compressive stress acting in the core, since all core displacement vectors are directed towards the center of the lattice. Furthermore, the coexistence of tensile and compressive stresses takes place

in shell regions. Indeed, it is remarked that the compressive stresses in the shell are located around the shell-core interface, while the tensile stresses occur near the shell surface, where the orientation of the displacement vectors changes along the shell lattice, which then slightly deforms. As a result, the system exhibits compressive but nonuniform stress along the $x$ and $y$ directions. When the HS shell lattice parameter is increased, as for $R_{0,S}^{\mathrm{HH}} = 1.04$ nm [Fig. 8(d)], a different stress distribution feature is obtained. The nanostructure displays coexisting regions of dilatational strain in the shell region and around the core-shell interface and weak compressive strain in the core. Indeed, the displacement field for the shell is outwards, i.e., the shell is expanding, while, at the same time for the core, the displacement is inwards, i.e., the core is experiencing contraction. As a consequence, one can easily identify a "circular" boundary wall of displacement fields formed between the core and shell lattice structure, varying in width along the corners and edges. This boundary wall formation clearly portrays the two different mechanisms going in the whole lattice structure at the same time. The first is the expansion of the shell lattice parameters at the stake of contraction in core lattice parameters. The second is the stabilization of the LS state in the core due to the contraction. Consequently, the transition temperature of the core lattice shifts to higher temperatures, which in turn also withholds the complete transition of the shell from LS to HS as can be seen in Fig. S.1 of SM [62]. Finally for $R_{0,S}^{\mathrm{HH}} = 1.05$ [Fig. 8(e)], a pure dilatational strain, acting everywhere in the lattice, stabilizes the HS state and decreases the spin transition temperatures of both moieties.

To confirm the previous conclusions drawn from the discussion of Fig. 8, we calculate the divergence and rotation of the displacement field, which corresponds to the trace of the strain tensor, describing the pure relative volume expansion, while the rotational part evidences the enhancement of the shear stresses. The spatial distribution of the divergence of the displacement field depicted in Fig. S.3 of SM [62] clearly shows a more or less homogenous distribution of the compressive stress inside the core for $R_{0S}^{\mathrm{HH}} \leqslant 1.04$ nm, which enhances for smaller $R_{0S}^{\mathrm{HH}}$ values. In contrast, for the case $R_{0S}^{\mathrm{HH}} = 1.05$ nm, the core experiences tensile stress in the plateau region due to no lattice misfit between the HS core and the HS shell which plays in favor of the HS state, which shifts the transition temperature downward, as we saw in Fig. 4.

## IV. CONCLUSION

This paper was devoted to the study of SCO nanostructures made of a core-shell nanoparticle, where both constituents are spin active and have different transition temperatures. To investigate the interplay between the magnetoelastic properties of these two subsystems which interact elastically through their common elastic interface, we adopted the case where the lattice parameters of the two constituents are the same in the LS state, and let them be different in the HS state. To realize this situation, we fixed the LS lattice parameter to 1.0 nm for the core and the shell, the HS lattice parameter of the core is set equal to 1.05 nm, and we change the HS shell parameter of the shell in the interval 1.00 and 1.05 nm. When HS core and shell lattice parameters are different, an elastic frustration takes place, which causes a significant shift of the transition temperature of the core, due to the compressive effect exerted by the shell.

Interestingly, while the thermal dependence of the shell is slightly affected by the previous changes, the lattice parameter is significantly impacted and shows a large temperature dependence which resembles that of the core part, which then, in turn, drives the elastic behavior of the shell. One of the most intriguing results emerging from the magnetoelastic interactions within the nanostructure concerns the reaction of the core. Indeed, for a strong lattice parameter misfit between the shell and core in HS, the shell shows thermally induced multistep transitions on both the HS fraction and lattice parameter. In contrast, the core exhibits a multistep transition on its lattice parameters but a simple transition on its HS fraction behavior. This type of behavior is impossible to obtain on a simple lattice.

Consequently, for the present specific case, the HS fraction of the core cannot be directly extracted from the behavior of the lattice parameter, and the fact that the lattice parameter converts in two steps does not mean that the spin transition has the same behavior. In addition, although the thermal dependence of the HS fraction of the core shows a single step transition, the corresponding average bond length exhibits multistep transitions, with plateau regions. Spatial self-organization of the spin states with labyrinth formation stabilizing longitudinal or transversal HS and LS strings, antiferromagnetically coupled to surrounding strings, is evidenced. This type of organization of the spin states deserves further investigations. Moreover, the case of a spin-crossover core-shell nanostructure, with core and shell having the same lattice parameter in the HS state and a lattice parameter misfit in the LS state, is also very interesting. According to the transition temperatures of each part, several situations can emerge on cooling from the HS state. This particular case is being studied and the results will be submitted in a separate work.

Finally, it should be noted that the core-shell structure is defined in a finite size, and thus the system does not have phase transitions which are defined in the thermodynamic limit. The transitions studied here give characteristic changes of physical quantities depending on the frustrated situation which may benefit from finite-size scaling investigations. It is worth mentioning that recent developments on the elastic studies of three-dimensional (3D) nanoparticles [65] open the way to interesting studies on 3D core-shell nanoparticles with the aim to investigate the role of the shape's effect and the magnetoelastic coupling at the interface on the thermodynamic properties of the switchable SCO nanostructures.

## ACKNOWLEDGMENTS

This work was supported by Centre National de la Recherche Scientifique; the universities of Versailles, Paris Saclay, and LIA (French Japan International Laboratory); and the French Ministère de la Recherche. The present paper was supported by Grants-in-Aid for Scientific Research C (Grants No. 17K05508 and No. 18K03444) from Ministry of Education, Culture, Sports, Science, and Technology of Japan.

[1] E. König, *Nature and Dynamics of the Spin-State Interconversion in Metal Complexes*, Vol. 76 (Springer, New York, 1991), p. 51.

[2] P. Gütlich, Spin crossover in iron(II) complexes, Struct. Bond. **44**, 83 (1981).

[3] S. Decurtins, P. Gütlich, K. M. Hasselbach, A. Hauser, and H. Spiering, Light-induced excited-spin-state trapping in iron(ii) spin-crossover systems: Optical spectroscopic and magnetic-susceptibility study, Inorg. Chem. **24**, 2174 (1985).

[4] H. Toftlund, Spin equilibria in iron(II) complexes, Coord. Chem. Rev. **94**, 67 (1989).

[5] C.P. Köhler, R. Jakobi, E. Meissner, L. Wiehl, H. Spiering, and P. Gütlich, Nature of the phase transition in spin crossover compounds, J. Phys. Chem. Solids **51**, 239 (1990).

[6] M.A. Halcrow, Structure: Function relationships in molecular spin-crossover complexes, Chem. Soc. Rev. **40**, 4119 (2011).

[7] O. Kahn, *Molecular Magnetism* (VCH-Verlag, Weinheim, New York, 1993).

[8] J. Zarembowitch and O. Kahn, ChemInform abstract: Spin transition molecular systems: Towards information storage and signal processing, New J. Chem. **22** (1991).

[9] O. Kahn, J. Kröber, and C. Jay, Spin transition molecular materials for displays and data recording, Adv. Mater. **4**, 718 (1992).

[10] J. Linares, E. Codjovi, and Y. Garcia, Pressure and temperature spin crossover sensors with optical detection, Sensors **12**, 4479 (2012).

[11] Y. Garcia, P. J. van Koningsbruggen, E. Codjovi, R. Lapouyade, O. Kahn, and L. Rabardel, Non-classical Fe-II spin-crossover behaviour leading to an unprecedented extremely large apparent thermal hysteresis of 270 K: Application for displays, J. Mater. Chem. **7**, 857 (1997).

[12] O. Kahn and C. J. Martinez, Spin-transition polymers: From molecular materials toward memory devices, Science **279**, 44 (1998).

[13] R.-J. Wei, Q. Huo, J. Tao, R.-B. Huang, and L.-S. Zheng, Spin-crossover Fe(II)4 squares: Two-step complete spin transition and reversible single-crystal-to-single-crystal transformation, Angew. Chemie Int. Ed. **50**, 8940 (2011).

[14] Y.-X. Wang, D. Qiu, S.-F. Xi, Z.-D. Ding, Z. Li, Y. Li, X. Ren, and Z.-G. Gu, Iron(ii)-triazole core–shell nanocomposites: Toward multistep spin crossover materials, Chem. Commun. **52**, 8034 (2016).

[15] C. Jureschi, J. Linares, A. Rotaru, and Y. Garcia, Multi-step in 3D spin crossover nanoparticles simulated by an Ising model using entropic sampling Monte Carlo technique, Magnetochemistry **2**, 13 (2016).

[16] D. Chiruta, C.-M. Jureschi, J. Linares, P. R. Dahoo, Y. Garcia, and A. Rotaru, On the origin of multi-step spin transition behaviour in 1D nanoparticles, Eur. Phys. J. B **88**, 233 (2015).

[17] E. Milin, S. Belaïd, V. Patinec, S. Triki, G. Chastanet, and M. Marchivie, Dinuclear spin-crossover complexes based on tetradentate and bridging cyanocarbanion ligands, Inorg. Chem. **55**, 9038 (2016).

[18] H. Fourati, E. Milin, A. Slimani, G. Chastanet, Y. Abid, S. Triki, and K. Boukheddaden, Interplay between a crystal's shape and spatiotemporal dynamics in a spin transition material, Phys. Chem. Chem. Phys. **20**, 10142 (2018).

[19] T. Kosone, I. Tomori, C. Kanadani, T. Saito, T. Mochida, and T. Kitazawa, Unprecedented three-step spin-crossover transition in new 2-dimensional coordination polymer $\{Fe^{II}(4\text{-methylpyridine})_2[Au^{I}(CN)_2]_2\}$, Dalt. Trans. **39**, 1719 (2010).

[20] M. Nihei, H. Tahira, N. Takahashi, Y. Otake, Y. Yamamura, K. Saito, and H. Oshio, Multiple bistability and tristability with dual spin-state conversions in $[Fe(dpp)_2][Ni(mnt)_2]_2{\cdot}MeNO_2$, J. Am. Chem. Soc. **132**, 3553 (2010).

[21] A. Kaiba, H. J. Shepherd, D. Fedaoui, P. Rosa, A. E. Goeta, N. Rebbani, J. F. Létard, and P. Guionneau, Crystallographic elucidation of purely structural, thermal and light-induced spin transitions in an iron(II) binuclear complex, Dalt. Trans. **39**, 2910 (2010).

[22] M. Seredyuk, K. O. Znovjyak, J. Kusz, M. Nowak, M. C. Muñoz, and J. A. Real, Control of the spin state by charge and ligand substitution: Two-step spin crossover behaviour in a novel neutral iron(II) complex, Dalt. Trans. **43**, 16387 (2014).

[23] H. P. Zhang, L. C. Yang, L. J. Fu, Q. Cao, D. L. Sun, Y. P. Wu, and R. Holze, Core-shell structured electrode materials for lithium ion batteries, J. Solid State Electrochem. **13**, 1521 (2009).

[24] G. Félix, W. Nicolazzi, L. Salmon, G. Molnár, M. Perrier, G. Maurin, J. Larionova, J. Long, Y. Guari, and A. Bousseksou, Enhanced Cooperative Interactions at the Nanoscale in Spin-Crossover Materials with a First-Order Phase Transition, Phys. Rev. Lett. **110**, 235701 (2013).

[25] H. J. Shepherd, G. Molnár, W. Nicolazzi, L. Salmon, and A. Bousseksou, Spin crossover at the nanometre scale, Eur. J. Inorg. Chem. **2013**, 653 (2013).

[26] A. Bousseksou, G. Molnár, L. Salmon, and W. Nicolazzi, Molecular spin crossover phenomenon: Recent achievements and prospects, Chem. Soc. Rev. **40**, 3313 (2011).

[27] A. Rotaru, F. Varret, A. Gindulescu, J. Linares, A. Stancu, J. F. Létard, T. Forestier, and C. Etrillard, Size effect in spin-crossover systems investigated by FORC measurements, for surfacted $[Fe(NH_2\text{-}trz)_3](Br)_2\,3H_2O$ nanoparticles: Reversible contributions and critical size, Eur. Phys. J. B **84**, 439 (2011).

[28] A. Carné, C. Carbonell, I. Imaz, and D. Maspoch, Nanoscale metal-organic materials, Chem. Soc. Rev. **40**, 291 (2011).

[29] R. M. van der Veen, O.-H. H. Kwon, A. Tissot, A. Hauser, and A. H. Zewail, Single-nanoparticle phase transitions visualized by four-dimensional electron microscopy, Nat. Chem. **5**, 395 (2013).

[30] A. Bousseksou, J. Nasser, J. Linares, K. Boukheddaden, and F. Varret, Ising-like model for the two-step spin-crossover, J. Phys. I France **2**, 1381 (1992).

[31] A. Atitoaie, R. Tanasa, A. Stancu, and C. Enachescu, Study of spin crossover nanoparticles thermal hysteresis using FORC diagrams on an Ising-like model, J. Magn. Magn. Mater. **368**, 12 (2014).

[32] T. Kawamoto and S. Abe, Thermal hysteresis loop of the spin-state in nanoparticles of transition metal complexes: Monte Carlo simulations on an Ising-like model, Chem. Commun. **31**, 3933 (2005).

[33] A. Muraoka, K. Boukheddaden, J. Linares, and F. Varret, Two-dimensional Ising-like model with specific edge effects for spin-crossover nanoparticles: A Monte Carlo study, Phys. Rev. B **84**, 054119 (2011).

[34] D. Chiruta, C.-M. Jureschi, J. Linares, Y. Garcia, and A. Rotaru, Lattice architecture effect on the cooperativity of spin transition coordination polymers, J. Appl. Phys. **115**, 053523 (2014).

[35] J. A. Nasser, First order high-spin/low-spin phase transition induced by acoustic-phonons, Eur. Phys. J. B **21**, 3 (2001).

[36] G. Félix, W. Nicolazzi, M. Mikolasek, G. Molnár, and A. Bousseksou, Non-extensivity of thermodynamics at the nanoscale in molecular spin crossover materials: A balance between surface and volume, Phys. Chem. Chem. Phys. **16**, 7358 (2014).

[37] H. Oubouchou, A. Slimani, and K. Boukheddaden, Interplay between elastic interactions in a core-shell model for spin-crossover nanoparticles, Phys. Rev. B **87**, 104104 (2013).

[38] M. Nishino, K. Boukheddaden, Y. Konishi, and S. Miyashita, Simple Two-Dimensional Model for the Elastic Origin of Cooperativity Among Spin States of Spin-Crossover Complexes, Phys. Rev. Lett. **98**, 247203 (2007).

[39] C. Enachescu, L. Stoleriu, A. Stancu, and A. Hauser, Elastic Relaxation Phenomena in Finite 2D Hexagonal Molecular Lattices, Phys. Rev. Lett. **102**, 257204 (2009).

[40] M. Mikolasek, W. Nicolazzi, F. Terki, G. Molnár, and A. Bousseksou, Surface transition in spin crossover nanoparticles, Chem. Phys. Lett. **678**, 107 (2017).

[41] M. Mikolasek, W. Nicolazzi, F. Terki, G. Molnár, and A. Bousseksou, Investigation of surface energies in spin crossover nanomaterials: The role of surface relaxations, Phys. Chem. Chem. Phys. **19**, 12276 (2017).

[42] C. Enachescu, R. Tanasa, A. Stancu, A. Tissot, J. Laisney, and M.-L. Boillot, Matrix-assisted relaxation in $Fe(phen)_2(NCS)_2$ spin-crossover microparticles, experimental and theoretical investigations, Appl. Phys. Lett. **109**, 031908 (2016).

[43] A. Slimani, H. Khemakhem, and K. Boukheddaden, Structural synergy in a core-shell spin crossover nanoparticle investigated by an electroelastic model, Phys. Rev. B **95**, 174104 (2017).

[44] L. Stoleriu, A. Stancu, P. Chakraborty, A. Hauser, and C. Enachescu, Analysis of first order reversal curves in the thermal hysteresis of spin-crossover nanoparticles within the mechanoelastic model, J. Appl. Phys. **117**, 17B307 (2015).

[45] A. Slimani, K. Boukheddaden, and K. Yamashita, Thermal spin transition of circularly shaped nanoparticles in a core-shell structure investigated with an electroelastic model, Phys. Rev. B **89**, 214109 (2014).

[46] A. Slimani, K. Boukheddaden, F. Varret, H. Oubouchou, M. Nishino, and S. Miyashita, Microscopic spin-distortion model for switchable molecular solids: Spatiotemporal study of the deformation field and local stress at the thermal spin transition, Phys. Rev. B **87**, 014111 (2013).

[47] A. Slimani, K. Boukheddaden, F. Varret, M. Nishino, and S. Miyashita, Properties of the low-spin high-spin interface during the relaxation of spin-crossover materials, investigated through an electro-elastic model, J. Chem. Phys. **139**, 194706 (2013).

[48] A. Slimani, K. Boukheddaden, and K. Yamashita, Effect of intermolecular interactions on the nucleation, growth, and propagation of like-spin domains in spin-crossover materials, Phys. Rev. B **92**, 014111 (2015).

[49] G. Félix, M. Mikolasek, G. Molnár, W. Nicolazzi, and A. Bousseksou, Tuning the spin crossover in nano-objects: From hollow to core-shell particles, Chem. Phys. Lett. **607**, 10 (2014).

[50] M. Mikolasek, G. Félix, G. Molnár, F. Terki, W. Nicolazzi, and A. Bousseksou, Role of surface vibrational properties on cooperative phenomena in spin-crossover nanomaterials, Phys. Rev. B **90**, 075402 (2014).

[51] G. Félix, M. Mikolasek, G. Molnár, W. Nicolazzi, and A. Bousseksou, Control of the phase stability in spin-crossover core-shell nanoparticles through the elastic interface energy, Eur. J. Inorg. Chem. **2018**, 435 (2018).

[52] A. C. Felts, A. Slimani, J. M. Cain, M. J. Andrus, A. R. Ahir, K. A. Abboud, M. W. Meisel, K. Boukheddaden, and D. R. Talham, Control of the speed of a light-induced spin transition through mesoscale core-shell architecture, J. Am. Chem. Soc. **140**, 5814 (2018).

[53] A. Tokarev, J. Long, Y. Guari, J. Larionova, F. Quignard, P. Agulhon, M. Robitzer, G. Molnár, L. Salmon, and A. Bousseksou, Spin crossover polysaccharide nanocomposites, New J. Chem. **37**, 3420 (2013).

[54] D. Qiu, D.-H. Ren, L. Gu, X.-L. Sun, T.-T. Qu, Z.-G. Gu, and Z. Li, Spin crossover-graphene nanocomposites: Facile syntheses, characterization, and magnetic properties, RSC Adv. **4**, 31323 (2014).

[55] L. Zhi-Hua, W. Yu-Xia, Q. Dan, L. Zai-Jun, and G. Zhi-Guo, AAO assisted 1D confined assembly and 2D surface filming of iron (II) triazole nanomaterial and spin-crossover properties, Chinese J. Inorg. Chem. **12**, 2311 (2017).

[56] C. Gatel, F. J. Bonilla, A. Meffre, E. Snoeck, B. Warot-Fonrose, B. Chaudret, L.-M. Lacroix, and T. Blon, Size-specific spin configurations in single iron nanomagnet: From flower to exotic vortices, Nano Lett. **15**, 6952 (2015).

[57] L.-M. Lacroix, N. Frey Huls, D. Ho, X. Sun, K. Cheng, and S. Sun, Stable single-crystalline body centered cubic Fe nanoparticles, Nano Lett. **11**, 1641 (2011).

[58] A. Adam, M. Poggi, E. Larquet, R. Cortès, L. Martinelli, P.-E. Coulon, E. Lahera, O. Proux, D. Chernyshov, K. Boukheddaden, T. Gacoin, and I. Maurin, Strain engineering of photo-induced phase transformations in Prussian blue analogue heterostructures, Nanoscale **10**, 16030 (2018).

[59] A. Slimani, F. Varret, K. Boukheddaden, C. Chong, H. Mishra, J. Haasnoot, and S. Pillet, Visualization and quantitative analysis of spatiotemporal behavior in a first-order thermal spin transition: A stress-driven multiscale process, Phys. Rev. B **84**, 094442 (2011).

[60] A. Slimani, F. Varret, K. Boukheddaden, D. Garrot, H. Oubouchou, and S. Kaizaki, Velocity of the High-Spin Low-Spin Interface Inside the Thermal Hysteresis Loop of a Spin-Crossover Crystal, Via Photothermal Control of the Interface Motion, Phys. Rev. Lett. **110**, 087208 (2013).

[61] P. Gütlich, A. Hausser, and H. Spiering, Thermal and optical switching of iron(II) complexes, Angew. Chem. **33**, 2024 (1994).

[62] See Supplemental Material at http://link.aps.org/supplemental/10.1103/PhysRevB.101.054105 for further plots of the variation of high-spin equilibrium lattice parameters of the shell, its effect on the core and shell spin fraction, the difference between the average and equilibrium of the core and shell lattice parameter in the high-spin state, and the divergence and rotation of the displacement field.

[63] H. Oubouchou, Y. Singh, and K. Boukheddaden, Magnetoelastic modeling of core-shell spin-crossover nanocomposites, Phys. Rev. B **98**, 014106 (2018).

[64] K. Boukheddaden, M. H. Ritti, G. Bouchez, M. Sy, M. M. Dîrtu, M. Parlier, J. Linares, and Y. Garcia, Quantitative contact pressure sensor based on spin crossover mechanism for civil security applications, J. Phys. Chem. C **122**, 7597 (2018).

[65] S. Laurentiu, N. Masamichi, S. Miyashita, A. Stancu, A. Hauser, and C. Enachescu, Cluster evolution in molecular three-dimensional spin-crossover systems, Phys. Rev. B **96**, 064115 (2017).